

Gate- and flux-tunable $\sin(2\varphi)$ Josephson element with proximitized Ge-based junctions

Axel Leblanc,^{1,*} Chotivut Tangchingchai,¹ Zahra Sadre Momtaz,² Elyjah Kiyooka,¹ Jean-Michel Hartmann,³ Frédéric Gustavo,¹ Jean-Luc Thomassin,¹ Boris Brun,¹ Vivien Schmitt,¹ Simon Zihlmann,¹ Romain Maurand,¹ Étienne Dumur,¹ Silvano De Franceschi,^{1,†} and François Lefloch^{1,‡}

¹*Univ. Grenoble Alpes, CEA, Grenoble INP, IRIG, PHELIQS, 38000 Grenoble, France*

²*Institut Néel, CNRS/UGA, Grenoble 38042, France*

³*Univ. Grenoble Alpes, CEA, LETI, 38000 Grenoble, France*

(Dated: June 18, 2024)

Hybrid superconductor-semiconductor Josephson field-effect transistors (JoFETs) function as Josephson junctions with a gate-tunable critical current. Additionally, they can feature a non-sinusoidal current-phase relation (CPR) containing multiple harmonics of the superconducting phase difference, a so-far underutilized property. In this work, we exploit this multi-harmonic property to create a Josephson circuit element with an almost perfectly π -periodic CPR, indicative of a largely dominant charge-4e supercurrent transport. Such a Josephson element was recently proposed as the basic building block of a protected superconducting qubit. Here, it is realized using a superconducting quantum interference device (SQUID) with low-inductance aluminum arms and two nominally identical JoFETs. The latter are fabricated from a SiGe/Ge/SiGe quantum-well heterostructure embedding a high-mobility two-dimensional hole gas. By carefully adjusting the JoFET gate voltages and finely tuning the magnetic flux through the SQUID close to half a flux quantum, we achieve a regime where the $\sin(2\varphi)$ component accounts for more than 95% of the total supercurrent. This result demonstrates a new promising route for the realization of superconducting qubits with enhanced coherence properties.

I. INTRODUCTION

Quantum information processing requires qubits with long coherence time enabling high fidelity quantum gates. Over the past two decades, superconducting circuits have led to the realization of quantum processors of ever-growing size made of qubits with steadily improving fidelities [1]. This way, superconducting qubits have become one of the most advanced physical platforms for quantum computing. Progress has been driven by material engineering and optimization, as well as by the development of new device concepts capable of providing a growing level of protection against noise sources in the environment [2–4]. Qubit protection against relaxation and dephasing processes can be granted from the symmetry properties of the qubit Hamiltonian. In this direction, a variety of possible solutions have been proposed and only partly explored [5–11]. One of the leading ideas is to create superconducting qubits whose two lowest energy states are associated with odd and even numbers of Cooper pairs in a superconducting island, respectively. Due to the different parity, these states are orthogonal to each other in both charge and phase space [12–19]. This type of parity-protected qubit requires a parity-preserving Josephson element that only allows the coherent transfer of correlated pairs of Cooper pairs, which translates into devising a Josephson circuit with a π -periodic, $\sin(2\varphi)$ current phase relation (CPR).

Some proposals to engineer such a $\sin(2\varphi)$ qubits rely on conventional $\sin(\varphi)$ Josephson junctions, either arranged into large arrays [14] or embedded in a superconducting quantum interference device (SQUID) together with extremely large inductances [15]. The practical realisation of these ideas is technologically challenging and some significant experimental progress was reported only recently [19]. Another approach is to leverage the multi-harmonic CPR and the gate tunability of superconductor(S)-semiconductor(Sm) Josephson field-effect transistors (JoFETs)[20–29]. Various signatures of $\sin(2\varphi)$ Josephson elements were recently reported [30–35] and harnessed to demonstrate some first experimental evidence of parity protection [16]. However, a direct measurement of a $\sin(2\varphi)$ CPR and precise quantitative evaluation of its harmonic purity and its tunability have been missing so far. These important aspects are addressed in the present work. Our experimental study takes advantage of a recently developed S-Sm platform based on SiGe/Ge/SiGe quantum-well heterostructures. We investigate the CPR of a SQUID embedding two gate-tunable Josephson junctions, in short a G-SQUID. We demonstrate ample gate and magnetic-flux control of the Josephson harmonic content. In particular, our quantitative analysis based on a fully comprehensive model of our circuit, reveals that the desired $\sin(2\varphi)$ (i.e. charge-4e) contribution to supercurrent can reach up to 95.2% of the total supercurrent at half flux quantum through the SQUID. This achievement is a significant step forward in the development and optimization of a semiconductor-based parity-protected qubit.

* E-mail: axel.leblanc@cea.fr

† E-mail: silvano.defranceschi@cea.fr

‡ E-mail: francois.lefloch@cea.fr

II. DEVICE AND MEASUREMENT SETUP

The G-SQUID (shown in Fig. 1a) consists of an aluminum superconducting loop with nearly symmetric arms embedding two nominally identical JoFETs fabricated out of a SiGe/Ge/SiGe quantum-well heterostructure. The compressively strained Ge quantum well lies 22 nm beneath the semiconductor surface and hosts a two-dimensional hole gas exhibiting a mobility of $10^5 \text{ cm}^2/\text{Vs}$ measured at a carrier density of $6 \times 10^{11} \text{ cm}^{-2}$. The two JoFETs, J_{N1} and J_{N2} , have a $1 \mu\text{m}$ -wide and a 300 nm -long Ge channel (for more details on the JoFETs see Suppl. S1). The G-SQUID is embedded in a second larger loop together with a wider, reference JoFET, J_W , ($10 \mu\text{m}$ -wide and 300 nm -long Ge channel), enabling a direct CPR measurement [20, 22, 36–41]. To this purpose, J_W is designed to have a critical current much larger than those of J_{N1} and J_{N2} . The small and large superconducting loops are locally flux biased by means of two $10 \mu\text{m}$ -wide and 50 nm -thick Al lines whose cross-talks have been calibrated *in-situ* and then implicitly compensated throughout the rest of the paper (see Suppl. S6).

Furthermore, we stress that the Al arms have small but non-negligible inductances, mostly of kinetic origin, that we label as L_1 , L_2 and L_W . As our later analysis will reveal, properly extracting the intrinsic harmonic content of the JoFET CPRs from the measurements requires taking these inductances into account. In the rest of the paper, all of the calculated curves are obtained using the circuit model shown in Fig. 1a (see Suppl. S2 for more details).

All measurements were performed in a dilution refrigerator at a base temperature of 38 mK . The fabrication process and the measurement methods are very similar to those discussed in [32, 42].

III. CHARACTERISATION OF THE INDIVIDUAL JOFETS

To access the individual DC transport characteristic of a given JoFET in such a parallel configuration, we purposely apply large positive gate voltages ($\approx 1.5 \text{ V}$) to the other JoFETs, thereby suppressing current flow through their respective arms. The resulting individual characteristics of J_W , J_{N1} and J_{N2} as a function of their respective gate voltages are shown on color scale in Figs. 1b-d, with the corresponding circuit measurement schematics displayed in the insets.

For all the JoFETs, the current at which the device switches from superconducting to normal state, close to the critical current I_C , is clearly visible as an abrupt change of the measured source-drain voltage drop from 0 to a finite value. The three JoFETs exhibit a similar behavior denoting consistent properties of the Ge channel and the superconducting contacts. In particular, we note that the two narrow JoFETs, designed to be identical, have very similar $I_C^{N1}(V_G^{N1})$ characteristics.

By varying the magnetic flux, Φ_1 , through the larger loop we can sequentially measure the CPR of each JoFET in the G-SQUID. To this aim, the reference JoFET, J_W , is biased at full accumulation ($V_G^W = -1.5 \text{ V}$) such that the necessary condition $I_C^W \gg I_C^{N1}, I_C^{N2}$ is fulfilled [36, 43]. To measure the J_{N1} (J_{N2}) CPR, we apply $V_G^{N1} = -0.6 \text{ V}$ ($V_G^{N2} = -1.5 \text{ V}$) while J_{N2} (J_{N1}) is pinched off by setting $V_G^{N2} = 1.5 \text{ V}$ ($V_G^{N1} = 1.5 \text{ V}$). The on-state voltages $V_G^{N1} = -0.6 \text{ V}$ and $V_G^{N2} = -1.5 \text{ V}$ are chosen to obtain equal amplitudes of the first CPR harmonic. As we shall see below, operating the G-SQUID at these gate voltages enables the suppression of the first harmonic by flux-induced destructive interference, hence leaving a dominant $\sin(2\varphi)$ component.

The measured CPRs are shown in Figs. 1e,f together with the respective Fourier transforms. A total of 15 flux periods were measured in order to ensure sufficient resolution of the harmonics in Fourier space. Each reported I_C data point represents the median value obtained from 10 measurements, with the light green area indicating ± 1 standard deviation. Both CPRs are clearly skewed and we distinguish up to five harmonics. This multi-harmonicity indicates a high transparency of the superconducting contacts, which is consistent with earlier observations with similar devices [30, 32]. Yet, as we shall discuss below, the higher harmonics, especially the fourth and fifth one, have largely enhanced amplitudes due to the finite inductance of the aluminum arms.

IV. $\text{SIN}(2\varphi)$ JOSEPHSON ELEMENT

With the two JoFETs J_{N1} and J_{N2} independently characterized, we now turn to the study of the G-SQUID CPR, once again using J_W as a reference. With the ultimate goal to engineer a $\sin(2\varphi)$ Josephson element, we symmetrize the G-SQUID by applying $V_G^{N1} = -0.6 \text{ V}$ and $V_G^{N2} = -1.5 \text{ V}$.

Figure 2a shows a measurement of the G-SQUID critical current as a function of Φ_1 and Φ_2 , the latter being the magnetic flux through the G-SQUID loop. This is the most important data set. We fit the entire two-dimensional plot to the circuit model shown in Fig. 1a, with fixed inductances of the Al arms (see Suppl. S1) and twelve free parameters accounting for the amplitudes of the first four harmonics of the three JoFETs (see Suppl. S2 for details). Interestingly, the fit yields negligible amplitudes for all the fourth-order harmonics, implying that only three harmonics per JoFET are sufficient to reproduce the data. This outcome apparently contrasts with the experimental data in Figs. 1e,f, where up to five harmonics can be distinguished for both J_{N1} and J_{N2} . The discrepancy arises from the finite inductances of the Al arms [41, 44]. We estimate $L_1 \approx L_2 \approx 50 \text{ pH}$ (i.e. 20 times smaller than the inductances of J_{N1} and J_{N2}) and $L_W \approx 210 \text{ pH}$. Even such relatively small inductances can significantly enhance the harmonic amplitudes. The enhancement becomes proportionally larger as the harmonic

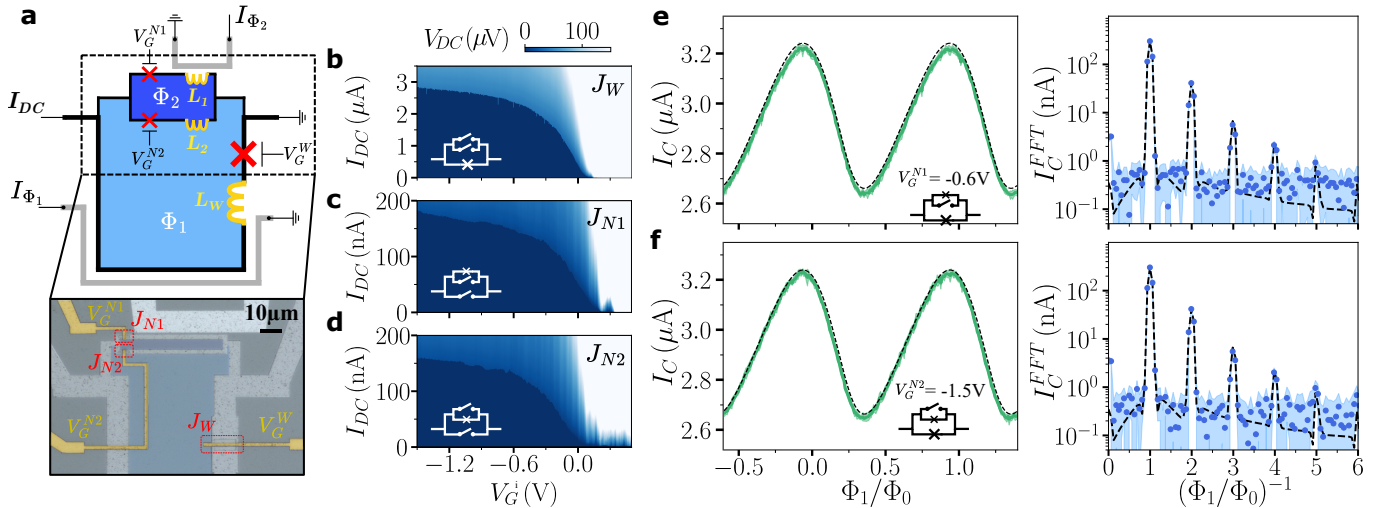


FIG. 1. **Double SQUID device and single-JoFET characteristics.** **a**, Schematic and scanning electron micrograph of the device. A Ge-based SQUID (G-SQUID), embedding JoFETs J_{N1} and J_{N2} , is connected in parallel to a wider JoFET (J_W) used as a reference Josephson junction for current-phase-relation (CPR) measurements. The aluminum arms are modeled by three inductances: L_1 , L_2 and L_W . **b,c,d**, Current-biased measurements of the JoFET characteristics for J_W , J_{N1} , and J_{N2} , respectively. In each panel, the measured source-drain voltage is plotted as a function of gate voltage, V_G^i ($i = W, N1, N2$), and source-drain current bias I_{DC} . **e** (resp. **f**), Left: critical current, I_C , as a function of magnetic flux Φ_1 through the large loop in **a**. The reference JoFET J_W is biased to strong accumulation ($V_G^W = -1.5V$), J_{N2} (resp. J_{N1}) is pinched off and $V_G^{N1} = -0.6V$ (resp. $V_G^{N2} = -1.5V$). The I_C oscillations are a direct measurement of J_{N2} (resp. J_{N1}) CPR. Right: Fast Fourier transform (FFT) of the CPR on the left, calculated over $15\Phi_0$. Dashed line: calculated FFT based on the circuit model in **a** with parameters obtained from a fit of the data in Fig. 2a.

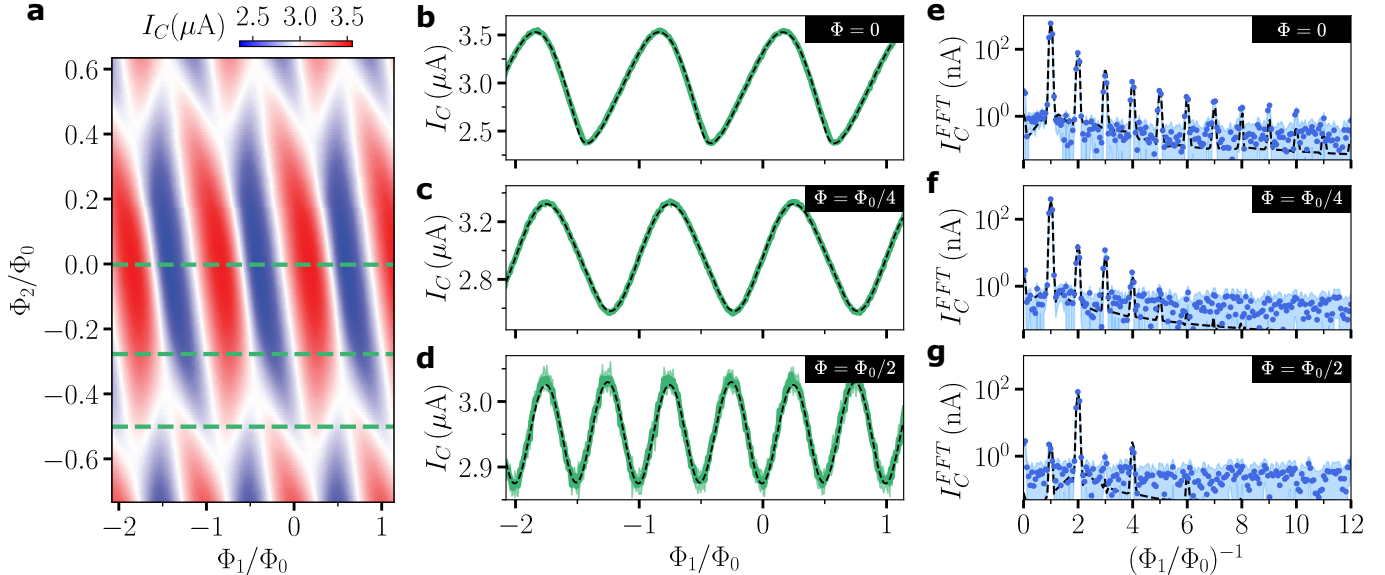


FIG. 2. **Frequency doubling of the G-SQUID CPR.** The G-SQUID is symmetrized by setting $V_G^{N1} = -1.5V$ and $V_G^{N2} = -0.6V$, which equalizes the amplitudes of the first harmonics in J_{N1} and J_{N2} . J_W is kept in strong accumulation ($V_G^W = -1.5V$). **a**, Critical current as a function of the two compensated magnetic fluxes, Φ_1 and Φ_2 , threading the large superconducting loop and the G-SQUID, respectively. **b,c,d**, G-SQUID CPR (I_C vs Φ_1) for $\Phi_2 = 0$, $\Phi_0/4$ and $\Phi_0/2$, i.e. at the line cuts denoted by green lines in **a**. **e,f,g**, the FFTs obtained from the CPRs in **b,c**, and **d**, respectively, are calculated over $15\Phi_0$. Dashed lines in **b,c,d** (**e,f,g**) are calculated FFTs based on the circuit model in Fig. 1a with parameters obtained from a fit of the data in **a**. In **d**, following a suppression of the odd harmonics (clearly shown in **d**), we observe the doubling of the CPR frequency as expected for a $\sin(2\varphi)$ Josephson element.

order increases [41, 44]. This aspect is fully captured by our circuit model. Indeed, the dashed lines in Figs. 1e,f are calculated using the parameters extracted from the fit of Fig. 2a. The experimental data are accurately reproduced despite the fact that only three harmonics effectively contribute to the CPR of each JoFET.

In Figs. 1e,f the arm inductances amplify the 1st, 2nd, and 3rd harmonics of J_{N1} (J_{N2}) by 7(6)%, 22(30)%, and 250(244)%, respectively, and lead to the emergence of a 4th and a 5th harmonic [45]. Hence our analysis reveals the importance of including even small contributions of arm inductances in order to avoid a crude overestimation of the harmonic amplitudes. Finally, we remark that arm inductances can also induce a phase shift in the CPR [44].

We finally address the magnetic-flux dependence of the G-SQUID CPR. At $\Phi_2 = 0$ (Figs. 2b,e), we expect the G-SQUID CPR to be the sum of the J_{N1} and J_{N2} CPRs shown in Figs. 1e,f. Instead, we observe a CPR containing about ten harmonics. Moreover, all harmonics beyond the first one exhibit amplitudes clearly larger than expected from a simple addition. Fully captured by our circuit model (see dashed lines in Figs. 2b,e), this finding is mostly a consequence of the moderate ratio between the critical current of the reference junction J_W and the one of the G-SQUID [43], i.e. $I_C^W/I_C^{G-SQUID} \approx 5$ at $\Phi_2 = 0$.

At $\Phi_2 = \Phi_0/4$ (Fig 2c,f), J_{N1} and J_{N2} are dephased by $\pi/2$, resulting in a destructive interference between even harmonics. The 2nd and 4th harmonics are consequently suppressed while the 1st and 3rd preserve the same amplitude. The resulting CPR is clearly less skewed than at $\Phi_2 = 0$. From our model, we conclude that the residual 2nd and 4th harmonics are again due to a moderate ratio $I_C^W/I_C^{G-SQUID}$. Increasing the J_W critical current by a factor ten would further suppress the 2nd harmonic by the same factor.

At $\Phi_2 = \Phi_0/2$ (Fig 2d,g), a π phase shift induces a destructive interference between the odd harmonics of J_{N1} and J_{N2} with reduction of the G-SQUID critical current. Following the suppression of the 1st and 3rd harmonics, the 2nd harmonic becomes the dominant one resulting in the emergence of a $\Phi_0/2$ flux periodicity in the CPR. In conclusion, at half flux quantum, the G-SQUID behaves as a $\sin(2\varphi)$ Josephson element.

V. HARMONIC TUNING AND $\sin(2\varphi)$ PURITY

Figure 2a shows how, in a symmetrized configuration with balanced Josephson junctions, the magnetic flux Φ_2 can profoundly change the harmonic composition of the G-SQUID CPR with singularities at $\Phi_2 = \pm\Phi_0/4$ and $\Phi_2 = \pm\Phi_0/2$. In order to gain more insight on this magnetic-flux control and to quantify the level of harmonic “distillation” at the singularity points, we show in Fig. 3a the complete Φ_2 dependence of the first four harmonics. The plotted amplitudes of these harmonics (colored dots) are extracted from Figure 2a by performing a Fourier transform of the measured $I_C(\Phi_1)$ at every Φ_2 value. The

corresponding uncertainties are represented by $\pm 1\sigma$ -wide colored bands. These uncertainties are significant and visible only when the harmonic amplitudes are below ~ 1 nA, which is always the case for the fourth harmonic.

The overlaid dashed lines represent the amplitudes of the first four harmonics calculated using the circuit model of Fig. 1a with model parameters obtained from the fitting of the data in Fig. 2a as previously discussed. The remarkable quantitative agreement over four orders of magnitude confirms the validity of our circuit model.

At $\Phi_2 = \pm\Phi_0/2$, the first and third harmonics exhibit cusp-like dips where their amplitude is suppressed by two orders of magnitude, while the second and fourth harmonics simultaneously attain local maxima. In particular, the amplitude of the second harmonic at $\Phi_2 = \pm\Phi_0/2$ is almost identical to the one at $\Phi_2 = 0$. We can define a “purity” level of the $\sin(2\varphi)$ CPR as the ratio between the second harmonic amplitude, $A_{2\varphi}$, and the sum of the four harmonic amplitudes, $\sum_n A_{n\varphi}$. Its flux dependence is displayed in Fig. 3b. At $\Phi_2 = \pm\Phi_0/2$, we reach a second-harmonic purity of $95.2 \pm 2.4\%$, largely exceeding the state-of-the-art [33, 35]. This already high purity level could be further increased by additional circuit optimization. On the one hand, based on the circuit model of Fig. 1a, our measurement underestimates the purity value due to the relatively small $I_C^W/I_C^{G-SQUID}$ ratio. We expect that a ten times larger $I_C^W/I_C^{G-SQUID}$ ratio would have resulted in a measured purity of 96.3%, much closer to the actual one. On the other hand, the intrinsic purity level could be increased by acting on other circuit parameters.

To illustrate that, we begin by noting that our fit of Fig. 2a reveals a slightly imperfect symmetry of the G-SQUID, quantified by a 0.7% discrepancy between the amplitudes of the first harmonics of J_{N1} and J_{N2} (see Supp. S2). Reducing this discrepancy to less than 0.14% is in principle possible through a fine adjustment of the gate voltages. This would increase the weight of the even harmonics to more than 99%, with the fourth harmonic accounting for a few percent of the total weight. We note that both the second and the fourth harmonics contribute to parity protection since they reflect the simultaneous transport of even numbers of Cooper pairs. As discussed before, the fourth harmonic is essentially absent in the CPR of the individual JoFETs, and it originates from the non-negligible inductance for G-SQUID arms. Based on our circuit model, we estimate that in a properly symmetrized G-SQUID, reducing the arm inductances L_1 and L_2 from 51 pH to 46 pH would largely suppress the fourth harmonic resulting in $\sin(2\varphi)$ purity above 99%.

Finally, at $\Phi_2 = \pm\Phi_0/4$ the contribution of the second harmonic goes down to $2.6 \pm 0.1\%$. This suppression of the second harmonic could be further pushed below 1% by changing the gate configuration (see Supp. S5).

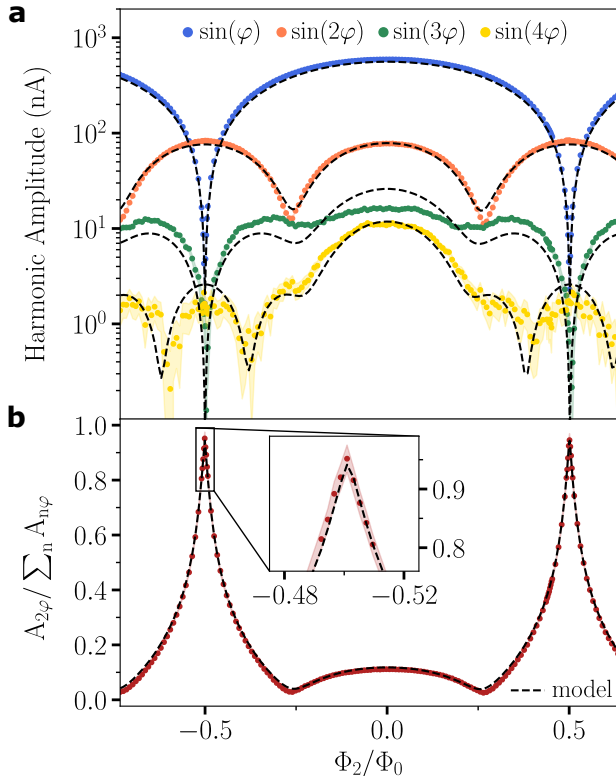


FIG. 3. **Flux modulation of the G-SQUID harmonics** **a**, Amplitudes of the first four harmonics in the G-SQUID CPR as a function of Φ_2 . The first harmonic vanishes at $\Phi_0/2$, while the second one vanishes at $\Phi_0/4$. **b**, Flux dependence of $\sin(2\varphi)$ purity, which is defined as the ratio between the amplitude of the second harmonic, $A_{2\varphi}$, and the sum of the all four harmonic amplitudes, $\Sigma_n A_{n\varphi}$. The $\sin(2\varphi)$ purity has a sharp maximum at $\Phi_0/2$ where it reaches $95.2 \pm 2.4\%$. Inset: close-up around the maximum. Colored bands in **a** and **b** represent the $\pm\sigma$ standard deviation originating from the experimental uncertainty on the CPR data points. Black dashed lines in **a** and **b** represent the harmonic amplitudes calculated from our circuit model using the fit parameters from of Fig. 2a.

VI. DISCUSSION AND CONCLUSIONS

Our study provides important insight to devise practical realizations of parity-protected qubit based on the demon-

strated $\sin(2\varphi)$ Josephson element [16, 17]. In principle, parity protection enhances the qubit lifetime at the cost of rendering the qubit resilient to external control pulses. Therefore, qubit operation would require temporarily exiting the protected regime, e.g. by controlling the ratio between the second and first harmonics. We show here that this ratio can be tuned by a magnetic flux or a gate voltage. A flux shift $\delta\Phi_2 = 0.025\Phi_0$ from $\Phi_2 = \Phi_0/2$ lower the second-harmonic content from 95% to 60%. In Supp. S4 we show that, starting from a symmetric biasing of the G-SQUID, a gate voltage shift $\delta V_G = 20$ mV in one of the two JoFETs lowers the $\sin(2\varphi)$ purity by about 25%. Such flux and gate-voltage shifts are experimentally accessible with electrical control pulses on the typical time scale (~ 10 ns) of single-qubit operations.

In conclusions, we have reported an experimental realization of a $\sin(2\varphi)$ Josephson element leveraging the intrinsic multi-harmonicity and gate tunability of SiGe-based JoFETs. The CPRs of these JoFETs can be accurately described by the sum of only three harmonics albeit higher harmonics are measured due to the relatively modest ratio between I_C^{ref} and I_C^{W} . The almost complete suppression of the odd harmonics at half a flux quantum leaves a $\sin(2\varphi)$ CPR with a remarkably high purity level exceeding 95%. We argued that even higher values beyond 99% could be reached through further circuit optimization. All data analysis was based on a relatively simple but accurate circuit model taking into account the non-sinusoidal CPRs of the JoFETs as well as the inductances of the superconducting arms.

ACKNOWLEDGMENTS

This work has been supported by the ANR project SUNISIDEuP (ANR-19-CE47-0010), the PEPR ROBUSTSUPERQ and PRESQUILE (ANR-22-PETQ-0003), the ERC starting grant LONGSPIN (Horizon 2020 - 759388) and the Grenoble LaBEX LANEF. We thank the PTA (CEA-Grenoble) for the nanofabrication. We thank J. Renard and S. Messelot for discussions.

[1] S. Bravyi, O. Dial, J. M. Gambetta, D. Gil, and Z. Nazario, The future of quantum computing with superconducting qubits, *Journal of Applied Physics* **132**, 160902 (2022).
 [2] A. Gyenis, A. Di Paolo, J. Koch, A. Blais, A. A. Houck, and D. I. Schuster, Moving beyond the Transmon: Noise-Protected Superconducting Quantum Circuits, *PRX Quantum* **2**, 030101 (2021).
 [3] A. Calzona and M. Carrega, Multi-mode architectures for noise-resilient superconducting qubits, *Superconductor*

Science and Technology **36**, 023001 (2022).
 [4] J. Danon, A. Chatterjee, A. Gyenis, and F. Kueemmeth, Protected solid-state qubits, *Applied Physics Letters* **119**, 260502 (2021).
 [5] B. Douçot and J. Vidal, Pairing of Cooper Pairs in a Fully Frustrated Josephson-Junction Chain, *Physical Review Letters* **88**, 227005 (2002).
 [6] A. Kitaev, Protected qubit based on a superconducting current mirror, arXiv:cond-mat/0609441 (2006).

- [7] J. Koch, T. M. Yu, J. Gambetta, A. A. Houck, D. I. Schuster, J. Majer, A. Blais, M. H. Devoret, S. M. Girvin, and R. J. Schoelkopf, Charge-insensitive qubit design derived from the Cooper pair box, *Physical Review A* **76**, 042319 (2007).
- [8] V. E. Manucharyan, J. Koch, L. I. Glazman, and M. H. Devoret, Fluxonium: Single Cooper-Pair Circuit Free of Charge Offsets, *Science* **326**, 113 (2009).
- [9] M. H. Devoret and R. J. Schoelkopf, Superconducting Circuits for Quantum Information: An Outlook, *Science* **339**, 1169 (2013).
- [10] K. Kalashnikov, W. T. Hsieh, W. Zhang, W.-S. Lu, P. Kamenov, A. Di Paolo, A. Blais, M. E. Gershenson, and M. Bell, Bifluxon: Fluxon-Parity-Protected Superconducting Qubit, *PRX Quantum* **1**, 010307 (2020).
- [11] A. Gyenis, P. S. Mundada, A. Di Paolo, T. M. Hazard, X. You, D. I. Schuster, J. Koch, A. Blais, and A. A. Houck, Experimental Realization of a Protected Superconducting Circuit Derived from the $0 - \pi$ Qubit, *PRX Quantum* **2**, 010339 (2021).
- [12] L. B. Ioffe and M. V. Feigel'man, Possible realization of an ideal quantum computer in Josephson junction array, *Physical Review B* **66**, 224503 (2002).
- [13] S. Gladchenko, D. Olaya, E. Dupont-Ferrier, B. Douçot, L. B. Ioffe, and M. E. Gershenson, Superconducting nanocircuits for topologically protected qubits, *Nature Physics* **5**, 48 (2009).
- [14] M. T. Bell, J. Paramanandam, L. B. Ioffe, and M. E. Gershenson, Protected Josephson Rhombus Chains, *Physical Review Letters* **112**, 167001 (2014).
- [15] W. C. Smith, A. Kou, X. Xiao, U. Vool, and M. H. Devoret, Superconducting circuit protected by two-Cooper-pair tunneling, *npj Quantum Information* **6**, 1 (2020).
- [16] T. W. Larsen, M. E. Gershenson, L. Casparis, A. Kringhøj, N. J. Pearson, R. P. G. McNeil, F. Kuemmeth, P. Krogstrup, K. D. Petersson, and C. M. Marcus, Parity-Protected Superconductor-Semiconductor Qubit, *Physical Review Letters* **125**, 056801 (2020).
- [17] C. Schrade, C. M. Marcus, and A. Gyenis, Protected Hybrid Superconducting Qubit in an Array of Gate-Tunable Josephson Interferometers, *PRX Quantum* **3**, 030303 (2022).
- [18] A. Maiani, M. Kjaergaard, and C. Schrade, Entangling Transmons with Low-Frequency Protected Superconducting Qubits, *PRX Quantum* **3**, 030329 (2022).
- [19] W. C. Smith, M. Villiers, A. Marquet, J. Palomo, M. R. Delbecq, T. Kontos, P. Campagne-Ibarcq, B. Douçot, and Z. Leghtas, Magnifying quantum phase fluctuations with Cooper-pair pairing, *Physical Review X* **12**, 021002 (2022), arXiv:2010.15488 [cond-mat, physics:quant-ph].
- [20] E. M. Spanton, M. Deng, S. Vaitiekėnas, P. Krogstrup, J. Nygård, C. M. Marcus, and K. A. Moler, Current-phase relations of few-mode InAs nanowire Josephson junctions, *Nature Physics* **13**, 1177 (2017).
- [21] C. D. English, D. R. Hamilton, C. Chialvo, I. C. Moraru, N. Mason, and D. J. Van Harlingen, Observation of nonsinusoidal current-phase relation in graphene Josephson junctions, *Physical Review B* **94**, 115435 (2016).
- [22] A. A. Golubov, M. Y. Kupriyanov, and E. Il'ichev, The current-phase relation in Josephson junctions, *Reviews of Modern Physics* **76**, 411 (2004).
- [23] C. W. J. Beenakker, Quantum transport in semiconductor-superconductor microjunctions, *Physical Review B* **46**, 12841 (1992).
- [24] K. Ueda, S. Matsuo, H. Kamata, Y. Sato, Y. Takeshige, K. Li, L. Samuelson, H. Xu, and S. Tarucha, Evidence of half-integer Shapiro steps originated from nonsinusoidal current phase relation in a short ballistic InAs nanowire Josephson junction, *Physical Review Research* **2**, 033435 (2020).
- [25] F. Nichele, E. Portolés, A. Fornieri, A. M. Whiticar, A. C. C. Drachmann, S. Gronin, T. Wang, G. C. Gardner, C. Thomas, A. T. Hatke, M. J. Manfra, and C. M. Marcus, Relating Andreev Bound States and Supercurrents in Hybrid Josephson Junctions, *Physical Review Letters* **124**, 226801 (2020).
- [26] G. Nanda, J. L. Aguilera-Servin, P. Rakyta, A. Kormányos, R. Kleiner, D. Koelle, K. Watanabe, T. Taniguchi, L. M. K. Vandersypen, and S. Goswami, Current-Phase Relation of Ballistic Graphene Josephson Junctions, *Nano Letters* **17**, 3396 (2017).
- [27] I. Sochnikov, L. Maier, C. A. Watson, J. R. Kirtley, C. Gould, G. Tkachov, E. M. Hankiewicz, C. Brüne, H. Buhmann, L. W. Molenkamp, and K. A. Moler, Nonsinusoidal Current-Phase Relationship in Josephson Junctions from the 3D Topological Insulator HgTe, *Physical Review Letters* **114**, 066801 (2015).
- [28] E. Portolés, S. Iwakiri, G. Zheng, P. Rickhaus, T. Taniguchi, K. Watanabe, T. Ihn, K. Ensslin, and F. K. de Vries, A tunable monolithic SQUID in twisted bilayer graphene, *Nature Nanotechnology* **17**, 1159 (2022).
- [29] C. Baumgartner, L. Fuchs, A. Costa, S. Reinhardt, S. Gronin, G. C. Gardner, T. Lindemann, M. J. Manfra, P. E. Faria Junior, D. Kochan, J. Fabian, N. Paradiso, and C. Strunk, Supercurrent rectification and magnetochiral effects in symmetric Josephson junctions, *Nature Nanotechnology* **17**, 39 (2022).
- [30] M. Valentini, O. Sagi, L. Baghumyan, T. de Gijssels, J. Jung, S. Calcaterra, A. Ballabio, J. Aguilera Servin, K. Aggarwal, M. Janik, T. Adletzberger, R. Seoane Souto, M. Leijnse, J. Danon, C. Schrade, E. Bakkers, D. Christina, G. Isella, and G. Katsaros, Parity-conserving Cooper-pair transport and ideal superconducting diode in planar germanium, *Nature Communications* **15**, 169 (2024).
- [31] C. Ciaccia, R. Haller, A. C. C. Drachmann, T. Lindemann, M. J. Manfra, C. Schrade, and C. Schönenberger, Charge-4e supercurrent in a two-dimensional InAs-Al superconductor-semiconductor heterostructure, *Communications Physics* **7**, 1 (2024).
- [32] A. Leblanc, C. Tangchingchai, Z. S. Momtaz, E. Kiyooka, J.-M. Hartmann, G. T. Fernandez-Bada, B. Brun-Barriere, V. Schmitt, S. Zihlmann, R. Maurand, É. Dumur, S. De Franceschi, and F. Lefloch, From nonreciprocal to charge-4e supercurrents in Ge-based Josephson devices with tunable harmonic content, arXiv:2311.15371 [cond-mat] (2023).
- [33] L. Banszerus, W. Marshall, C. W. Andersson, T. Lindemann, M. J. Manfra, C. M. Marcus, and S. Vaitiekėnas, Voltage-controlled synthesis of higher harmonics in hybrid Josephson junction circuits, arXiv:2402.11603 [cond-mat] (2024).
- [34] G. de Lange, B. van Heck, A. Bruno, D. J. van Woerkom, A. Geresdi, S. R. Plissard, E. P. A. M. Bakkers, A. R. Akhmerov, and L. DiCarlo, Realization of Microwave Quantum Circuits Using Hybrid Superconducting-Semiconducting Nanowire Josephson Elements, *Physical Review Letters* **115**, 127002 (2015).
- [35] S. Messelot, N. Aparicio, E. de Seze, E. Eyraud, J. Coraux,

- K. Watanabe, T. Taniguchi, and J. Renard, Direct measurement of a $\sin(2\varphi)$ current phase relation in a graphene superconducting quantum interference device, arXiv:2405.13642 [cond-mat] (2024).
- [36] M. L. Della Rocca, M. Chauvin, B. Huard, H. Pothier, D. Esteve, and C. Urbina, Measurement of the Current-Phase Relation of Superconducting Atomic Contacts, *Physical Review Letters* **99**, 127005 (2007).
- [37] A. Murani, A. Kasumov, S. Sengupta, Y. A. Kasumov, V. T. Volkov, I. I. Khodos, F. Brisset, R. Delagrèze, A. Chepelianskii, R. Deblock, H. Bouchiat, and S. Guéron, Ballistic edge states in Bismuth nanowires revealed by SQUID interferometry, *Nature Communications* **8**, 15941 (2017).
- [38] M. J. A. Stoutimore, A. N. Rossolenko, V. V. Bolginov, V. A. Oboznov, A. Y. Rusanov, D. S. Baranov, N. Pugach, S. M. Frolov, V. V. Ryazanov, and D. J. Van Harlingen, Second-Harmonic Current-Phase Relation in Josephson Junctions with Ferromagnetic Barriers, *Physical Review Letters* **121**, 177702 (2018).
- [39] M. Endres, A. Kononov, H. S. Arachchige, J. Yan, D. Mandrus, K. Watanabe, T. Taniguchi, and C. Schönberger, Current-Phase Relation of a WTe_2 Josephson Junction, *Nano Letters* **23**, 4654 (2023).
- [40] S. M. Frolov, *Current-Phase Relations of Josephson Junctions with Ferromagnetic Barriers*, Ph.D. thesis (2005).
- [41] L. V. Ginzburg, I. E. Batov, V. V. Bol'ginov, S. V. Egorov, V. I. Chichkov, A. E. Shchegolev, N. V. Klenov, I. I. Soloviev, S. V. Bakurskiy, and M. Y. Kupriyanov, Determination of the Current-Phase Relation in Josephson Junctions by Means of an Asymmetric Two-Junction SQUID, *JETP Letters* **107**, 48 (2018).
- [42] J.-M. Hartmann, N. Bernier, F. Pierre, J.-P. Barnes, V. Mazzocchi, J. Krawczyk, G. Lima, E. Kiyooka, and S. D. Franceschi, Epitaxy of Group-IV Semiconductors for Quantum Electronics, *ECS Transactions* **111**, 53 (2023).
- [43] I. Babich, A. Kudriashov, D. Baranov, and V. S. Stolyarov, Limitations of the Current-Phase Relation Measurements by an Asymmetric dc-SQUID, *Nano Letters* **23**, 6713 (2023).
- [44] F. Lecocq, *Dynamique Quantique Dans Un dcSQUID : Du Qubit de Phase à l'oscillateur Quantique Bidimensionnel*, These de doctorat, Grenoble (2011).
- [45] From our model we conclude that the 4th harmonic is completely due to branch inductances, .
- [46] D. C. Mattis and J. Bardeen, Theory of the Anomalous Skin Effect in Normal and Superconducting Metals, *Physical Review* **111**, 412 (1958).
- [47] M. Tinkham, *Introduction to Superconductivity*, 2nd ed., Dover Books on Physics (Mineola, NY, 2015).
- [48] D. Willsch, D. Rieger, P. Winkel, M. Willsch, C. Dickel, J. Krause, Y. Ando, R. Lescanne, Z. Leghtas, N. T. Bronn, P. Deb, O. Lanes, Z. K. Mineev, B. Dennig, S. Geisert, S. Günzler, S. Ihssen, P. Paluch, T. Reisinger, R. Hanna, J. H. Bae, P. Schüffelgen, D. Grützmacher, L. Buimagarinca, C. Morari, W. Wernsdorfer, D. P. DiVincenzo, K. Michielsen, G. Catelani, and I. M. Pop, Observation of Josephson harmonics in tunnel junctions, *Nature Physics* , 1 (2024).
-

Gate and flux tunable $\sin(2\varphi)$ Josephson element in proximitized junctions

Supplemental Materials

S-I. JOFET GEOMETRY AND ARM INDUCTANCES

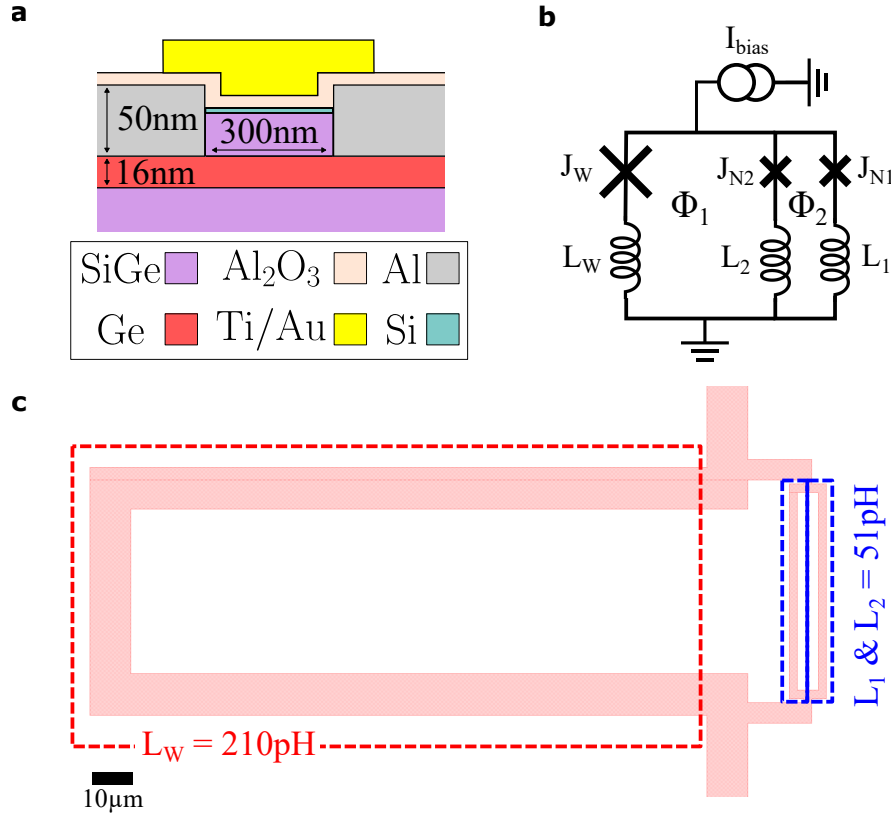


FIG. S1. **JoFET geometry and equivalent circuit of the double SQUID including arm inductances.** **a**, Cross-sectional sketch of a JoFET in which the Ge quantum well is contacted by two superconducting aluminum leads. The Ti/Au top gate allows tuning the hole carrier density in the channel. **b**, J_{N1} , J_{N2} and J_W are the JoFETs, L_1 , L_2 and L_3 are the inductances of the three aluminum arms. The device is current biased by I_{bias} . **c**, Design of the 3 aluminum arms with their respective inductances calculated by finite element simulation using the Sonnet software.

The inductances L_1 , L_2 and L_W have a geometric and a kinetic contribution L_{geo} and L_{kin} . The kinetic inductance per square L_{kin}^S is estimated from the aluminum normal state sheet resistance $R_S = 0.87 \Omega$ and its superconducting critical temperature $T_C = 1.5 \text{ K}$ (both measured on the same chip) [46, 47]:

$$L_{kin}^S \approx \frac{\hbar}{\pi} \frac{R_S}{1.76 k_B T_C} \quad (\text{S1})$$

where k_B is the Boltzmann constant. We find $L_{kin}^S = 0.8 \text{ pH sq}^{-1}$. To estimate the total loop inductance $L = L_{kin} + L_{geo}$, we use a finite element simulation performed in Sonnet and find $L_1 \& L_2 = 51 \text{ pH}$ and $L_W = 210 \text{ pH}$.

The inductance of the G-SQUID loop and the presence of higher harmonics in the junction CPR both lead to skewness in the I_C versus Φ data.

S-II. I_C VS Φ MODEL WITH INDUCTANCE

A. Theoretical model

To model the device behaviour we approximate the CPR of junction X (with $X \in \{W, N1, N2\}$) by a sum of n sinusoidal harmonics:

$$I_X(\varphi) = \sum_n (-1)^{n-1} H_n^X \sin(n\varphi) \quad (\text{S2})$$

where H_n^X is the magnitude of the n^{th} harmonic. We note φ_W , φ_{N1} and φ_{N2} the phases across each junction. Thus the overall current, I_{tot} , flowing through the device satisfies the following equation:

$$I_{tot}(\varphi_W, \varphi_{N1}, \varphi_{N2}) = I_W(\varphi_W) + I_{N1}(\varphi_{N1}) + I_{N2}(\varphi_{N2}) \quad (\text{S3})$$

Each arm of the double SQUID device contains an inductance (denoted $L1$, $L2$, and $L3$) and the two loops are flux biased by fluxes Φ_1 and Φ_2 , as depicted in Fig. S1. Consequently, the fluxoid quantification yields the following relations:

$$\varphi_{N2} = \varphi_W + \frac{2\pi}{\Phi_0} [L_W I_W(\varphi_W) - L_2 I_{N2}(\varphi_{N2}) + \Phi_1] \quad (\text{S4})$$

$$\varphi_{N1} = \varphi_{N2} + \frac{2\pi}{\Phi_0} [L_2 I_{N2}(\varphi_{N2}) - L_1 I_{N1}(\varphi_{N1}) + \Phi_2] \quad (\text{S5})$$

In order to ascertain the critical current of the device, it is necessary to identify the maximum supercurrent I_{tot} for which there exists a phase configuration $\{\varphi_W, \varphi_{N1}, \varphi_{N2}\}$ that satisfies S3,4 and 5. To this end, we must incorporate this additional information into our equation system:

$$\frac{\partial I_W}{\partial \varphi_W} = 0 \quad \frac{\partial I_{N1}}{\partial \varphi_{N1}} = 0 \quad \frac{\partial I_{N2}}{\partial \varphi_{N2}} = 0 \quad (\text{S6})$$

Consequently, the equation system S3,4,5, and 6 can be solved numerically to determine the critical current of the device at any flux configuration Φ_1, Φ_2 .

B. Fit to the model

The aforementioned model is employed to fit the G-SQUID flux response depicted in Fig. 2a. The resulting harmonic composition of the fit is shown in Fig. S2a. The arm inductances are fixed to the values estimated in S1, and the harmonic composition resulting from the fit is reported in Table S1. For purposes of comparison, the same model is also shown in Fig. S2b, with the harmonic amplitudes fixed to the values measured in Fig. 1e,f.

Parameter	L_1	L_2	L_W	H_1^W	H_2^W	H_3^W	H_4^W	H_1^{N1}	H_2^{N1}	H_3^{N1}	H_4^{N1}	H_1^{N2}	H_2^{N2}	H_3^{N2}	H_4^{N2}
Value	51pH	51pH	210pH	3.04 μ A	174nA	116nA	0nA	282.6nA	31.8nA	1.6nA	0nA	284.6nA	32.0nA	1.6nA	0nA
Fit	fixed	fixed	fixed	free	free	free	free	free	free	free	free	free	free	free	free
Error	N/A	N/A	N/A	0.03%	3.18%	1.14%	N/A	0.02%	0.18%	3.51%	N/A	0.02%	0.18%	3.48%	N/A

TABLE S1. **Fitting parameters considering the full model and the inductances from S1** The result is plotted in Fig. S2a.

Parameter	L_1	L_2	L_W	H_1^W	H_1^{N1}	H_2^{N1}	H_3^{N1}	H_4^{N1}	H_1^{N2}	H_2^{N2}	H_3^{N2}	H_4^{N2}
value	51pH	51pH	210pH	2.9 μ A	303.2nA	41nA	5.6nA	2.12nA	302.9nA	41.46nA	5.5nA	2.03nA
fit	fixed	fixed	fixed	fixed	fixed	fixed	fixed	fixed	fixed	fixed	fixed	fixed

TABLE S2. **Full model with inductances from S1 and harmonics amplitudes from measurements Fig. 1e,f.** The result is plotted in Fig. S2b.

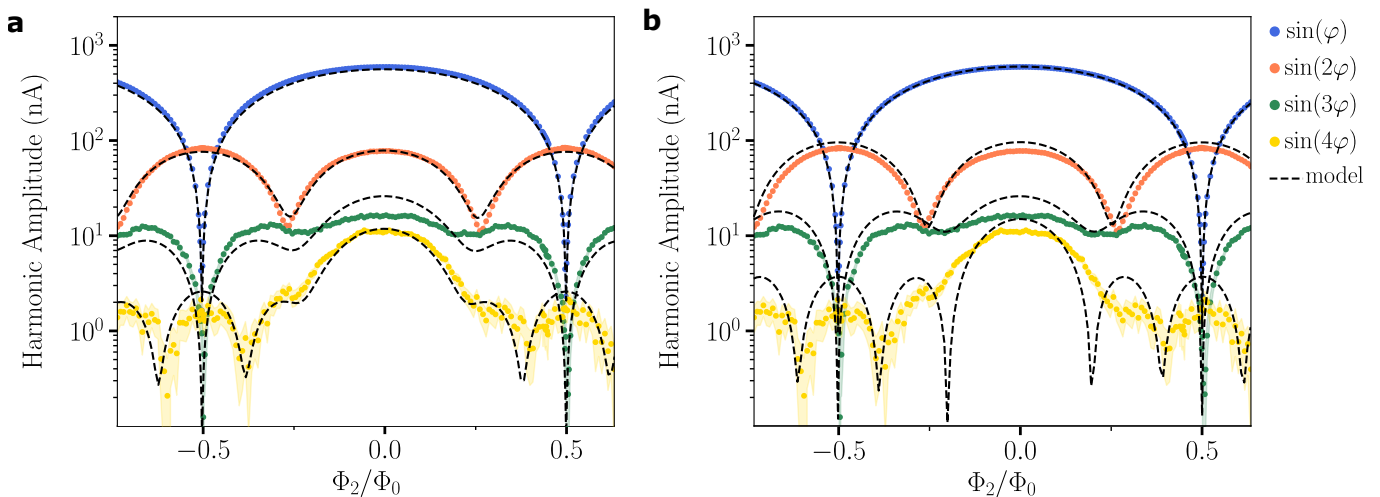


FIG. S2. **Model including arm inductances.** **a**, Model including the inductances from S1 while the JJs harmonic contents (reported in table S1) are given by the fit. **b**, Model including the inductances from S1 while the JJs harmonic contents are set to those measured in Fig. 1e,f (reported in Table S2).

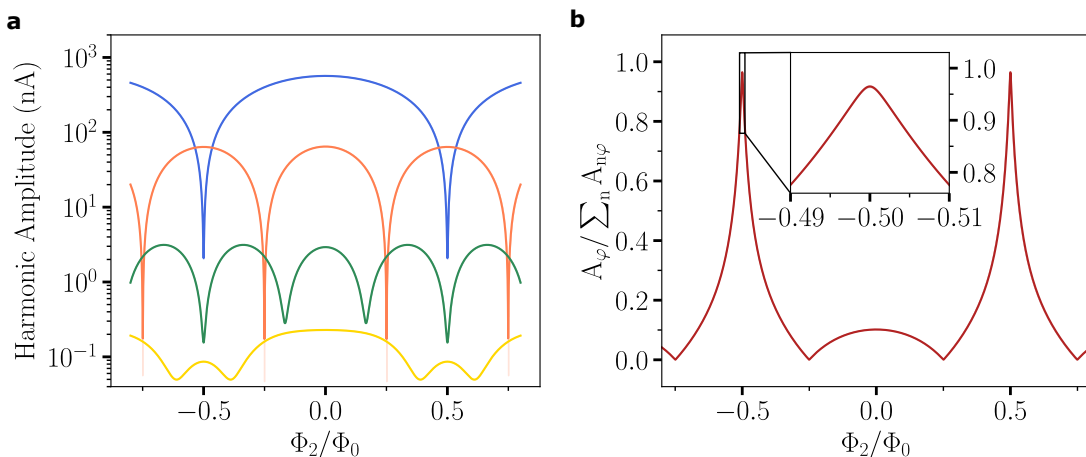


FIG. S3. **Theoretical G-SQUID CPR in the absence of arm inductances.** The junctions CPR compositions are obtained from the fit shown in Fig. S2a and listed in Table S2. The confidence interval provided by the fit, along with the correlation matrix, is employed to compute the confidence interval of the G-SQUID CPR composition, which is found to be negligible. **a**, Resulting G-SQUID harmonics amplitude as a function of flux threading Φ_2 . **b**, Associated $\sin(2\varphi)$ purity.

It can be observed that the inclusion of arm inductances in the model, while maintaining the harmonic content as measured in Fig. 1e,f, is insufficient to accurately reproduce the data. However, by fitting the data with the model, it is possible to identify a set of parameters (i.e., the harmonic content of each junction) that closely aligns with the experimental results.

Furthermore, the fit has enabled the determination of the "real" harmonic content of each junction. This allows for the estimation of the theoretical harmonic content of the G-SQUID in the absence of arm inductance. With a simple SQUID model without inductance, the G-SQUID harmonic content is obtained, as shown in Fig. S3. This theoretical harmonic content is comparable to the measured one, with the exception that the fourth harmonic is considerably smaller. Consequently, we can conclude that in this ideal situation, the $\sin(2\varphi)$ purity, which reaches 96.5%, cannot be limited by the presence of a fourth harmonic that is not suppressed at $\Phi_2 = \Phi_0/2$. Therefore, the remaining limiting parameter to reach the perfect $\sin(2\varphi)$ regime is the G-SQUID symmetry, in particular the symmetry of the first and third harmonics.

It is important to note that in order to accurately measure very high $\sin(2\varphi)$ purity using a double SQUID device, it is essential to consider the ratio between the reference junction and the G-SQUID critical currents. This ratio must be sufficiently large to prevent any artificial limitation on the figure of merit by enhancing higher order harmonics. This limitation can be illustrated by the G-SQUID CPR measured at $\Phi_2 = 0$ and shown in Fig. 2b. The CPR exhibits

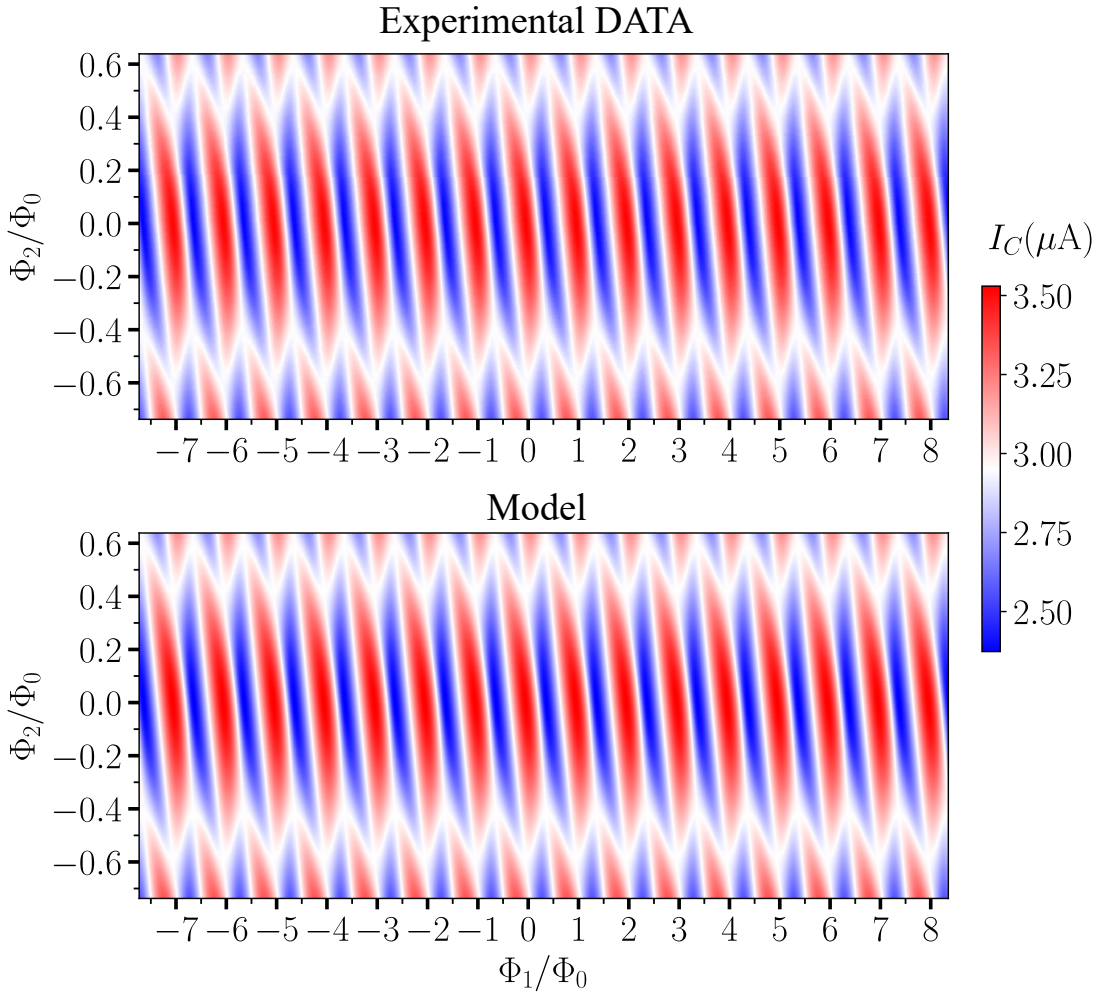


FIG. S4. **Full data set fit.** **Top panel**, Full Φ_1 VS Φ_2 data set (i.e. zoom out of Fig. 2a). **Lower panel**, Result from the fit using the full model described above and the fit parameters shown in Tab. S1.

sharp corners in the minima and smooth maxima, thereby breaking the time-reversal symmetry. This is an artefact resulting from the mixing of the reference junction and G-SQUID CPRs, which is made possible by a too small ratio I_C^{ref}/I_C^{SQUID} when $\Phi_2 = 0$. For further details, please refer to the detailed analysis presented in [43]. However, this artifact disappears around the point of interest, $\Phi_2 = \Phi_0/2$, since the ratio I_C^{ref}/I_C^{SQUID} is greater than 20 for this flux.

S-III. HARMONICS PHASES

In the main text, the harmonics of the G-SQUID CPR are extracted by Fourier transformation, and their respective absolute amplitudes are shown in Fig.3. Here, we show in Fig. S4 the phase of each harmonic as a function of the flux biasing the G-SQUID. The behaviors of these harmonics are well reproduced by the model described in Supp. S2 and shown with black dotted lines. The flux Φ_2 threading the G-SQUID dictates the phase difference across the G-SQUID. Consequently, the average slope of the n^{th} harmonic phase with respect to Φ_2 is:

$$\frac{\partial \varphi_n}{\partial \Phi_2} = n\pi\Phi_0 \quad (\text{S7})$$

Furthermore, each time the n^{th} harmonic is canceled (i.e. dips in Fig.3), its phase experience a π shift.

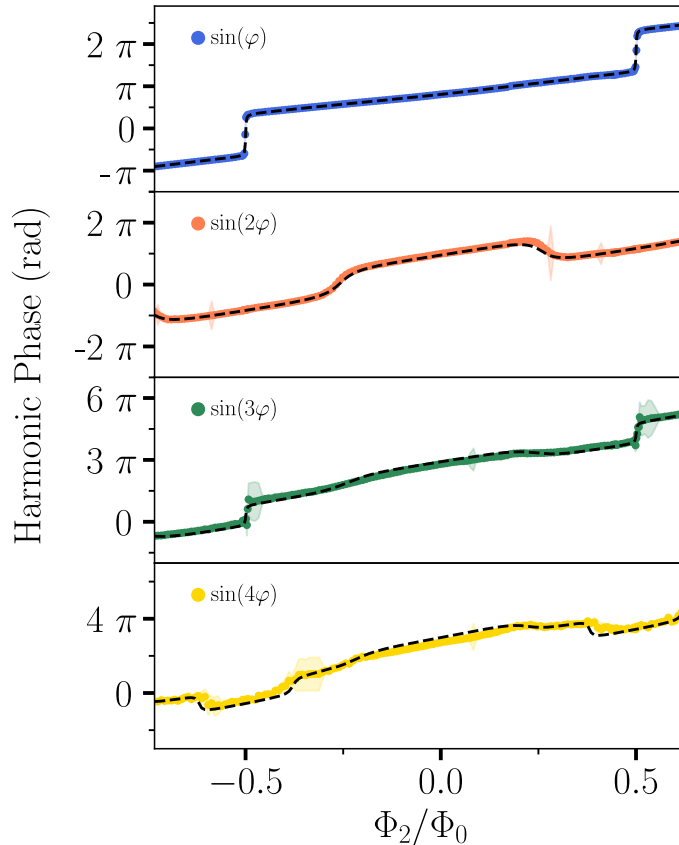


FIG. S5. **Flux dependence of harmonics phases.** The phase of each harmonic of the G-SQUID CPR extracted by Fourier transformation. The aforementioned phases are presented as a function of the flux Φ_2 threading the G-SQUID. The black dotted lines represent the phases extracted by the same methodology from the model discussed in Supp. S2.

S-IV. GATE TUNING OF G-SQUID SYMMETRY

We demonstrated the flux dependence of the harmonic content of the symmetric G-SQUID CPR. An alternative method for exiting the "sin(2 φ)" regime is to detune the G-SQUID from symmetry. In this experiment, the flux through the SQUID was set to $\Phi_2 = \Phi_0/2$.

In the initial stage of the experiment, the J_{N2} gate voltage was set to $V_G^{N2} = -1.5$ V in order to maintain a full accumulation, while the J_{N1} gate voltage was varied as illustrated in Fig. S5a. In Fig. S5b, we identify the reduction of the first harmonic around $V_G^{N1} = 0.7$ V. Consequently, this gate configuration corresponds to the symmetric G-SQUID regime. Figure S5c illustrates the phase evolution of each harmonic of the G-SQUID CPR. It can be observed that even harmonics maintain a constant phase, while a π shift occurs in odd phases around the symmetric regime point (see Supp. S4).

In a second instance, we examine a configuration where the G-SQUID symmetry is more susceptible to gate voltage. The gate voltage of J_{N2} is fixed at a value of $V_G^{N2} = -0.2$ V, while the gate voltage of J_{N1} is ramped between -0.3 V and 0.25 V, as indicated in Fig. S5d. As illustrated in Fig. S5e, the harmonic dependence of the gate is more pronounced in this configuration than in the previous one. In such a configuration, we demonstrate that a gate voltage shift of 20 mV on V_G^{N1} permits the achievement of a purity shift from 91% to 67% .

S-V. SECOND HARMONIC CANCELING

In the main text, we focused on the cancellation of the first harmonic in order to engineer a CPR dominated by the second harmonic. To do so the gate configuration was chosen to equalize the first harmonics of the two junctions of the G-SQUID because the more symmetric they are, the more they are cancelled out at $\Phi_2 = \Phi_0/2$. In this section, we investigate the suppression of the second harmonic and choose a suitable gate configuration: $V_G^{N1} = -0.15$ V and $V_G^{N2} = -1.5$ V. Figure S6a shows the resulting CPR as function of Φ_2 . Line cuts and Fourier transforms (Fig. S6b,c,d,e,f,g) highlight the CPR at $\Phi_2 = 0$, $\Phi_2 = \Phi_0/4$ and $\Phi_2 = \Phi_0/2$. It is observed that the second harmonic is completely suppressed at $\Phi_0/4$, but that the first harmonic is no longer completely canceled at $\Phi_0/2$. This is due to the fact that we cannot reach perfect symmetry in the G-SQUID for both first and second harmonics.

Fig. S7 shows the amplitudes and phases of each harmonic with respect to the flux Φ_2 threading the G-SQUID. The lower panel of Fig. S7a shows the first harmonic purity defined as ratio between the first harmonic amplitude and the total supercurrent amplitude. The maximum value reported is $97.3 \pm 0.6\%$. It is noteworthy that this range of sin(φ) purity is comparable to state of the art aluminum tunnel junctions as recently reported by Willsch et al. [48].

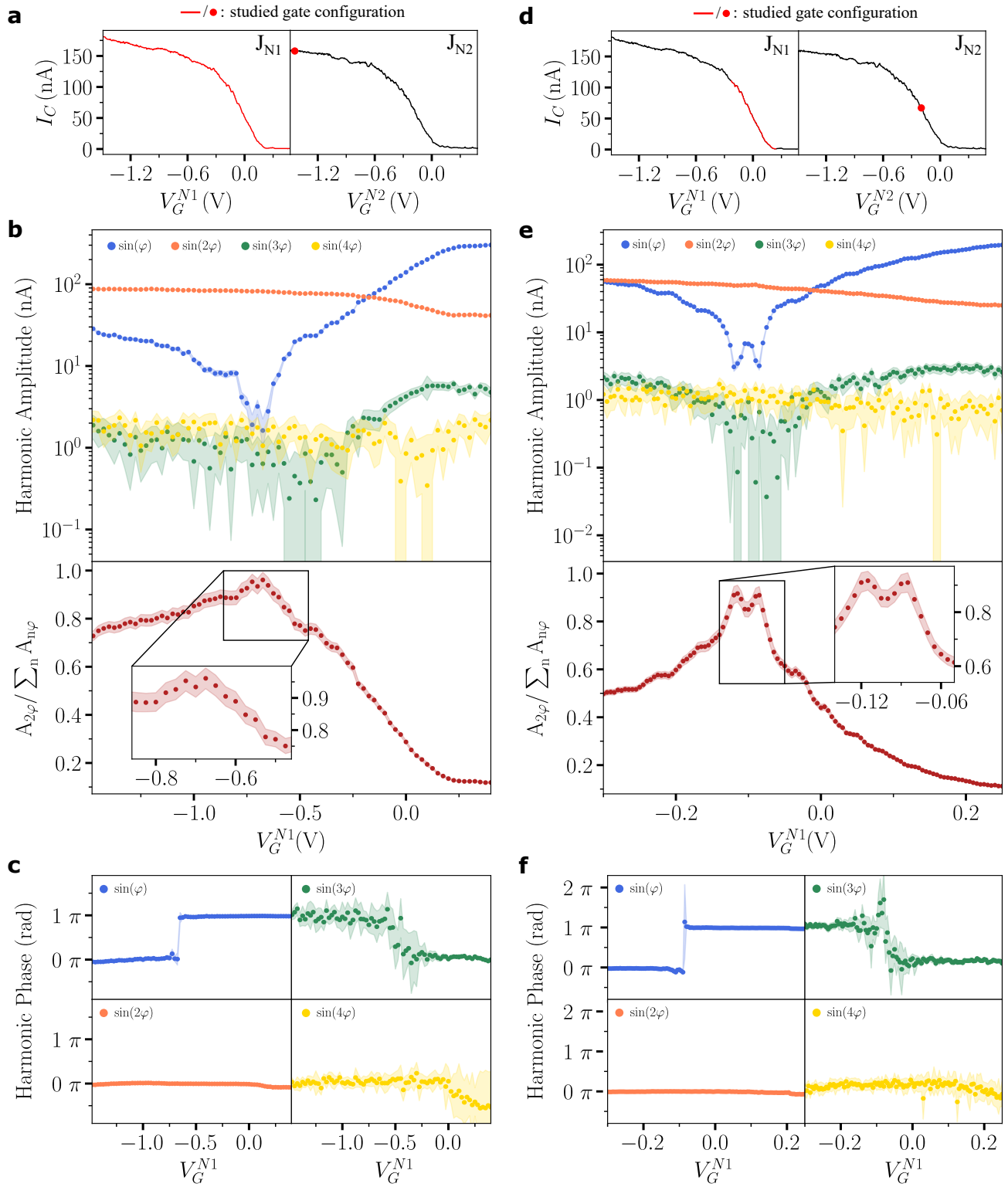


FIG. S6. **Gate modulation of the G-SQUID CPR.** The left column depicts the gate modulation in the high accumulation regime, while the right column illustrates it in the lower accumulation. **a[d]**, Gate configurations explored: The J_{N1} gate voltage is swept along the red line (left panel) while the J_{N2} gate voltage is maintained at the value represented by the red point (right panel). **b[e]**, amplitudes of the four first harmonics (top panel) and the $\sin(2\varphi)$ purity (bottom panel) with respect to the J_{N1} gate voltage. **c[f]**, phases of the four first harmonics with respect to the J_{N1} gate voltage.

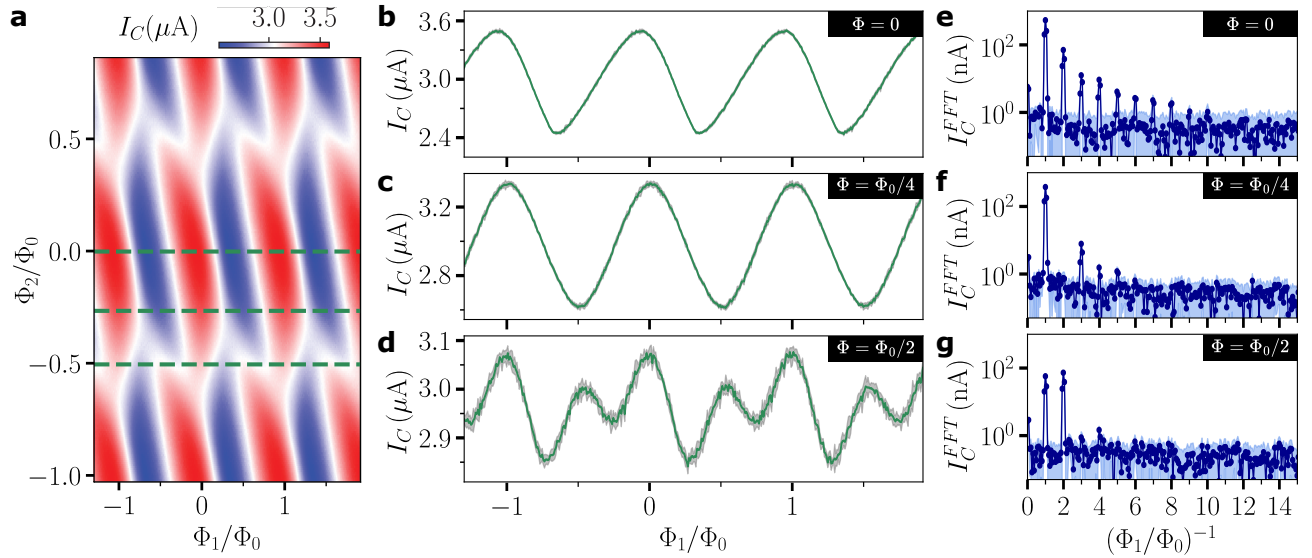


FIG. S7. **Second harmonic cancellation.** The G-SQUID is tuned to make the second harmonics symmetric and thus maximize their cancellation at $\Phi_0/4$: $V_G^{N1} = -0.15$ V and $V_G^{N2} = -1.5$ V **a**, Critical current as a function of both fluxes Φ_1 and Φ_2 revealing the G-SQUID CPR. **b**[**c**][**d**], CPR at $\Phi_2 = 0$ [$\Phi_2 = \Phi_0/4$] [$\Phi_2 = \Phi_0/2$] and its Fourier decomposition **e**[**f**][**g**].

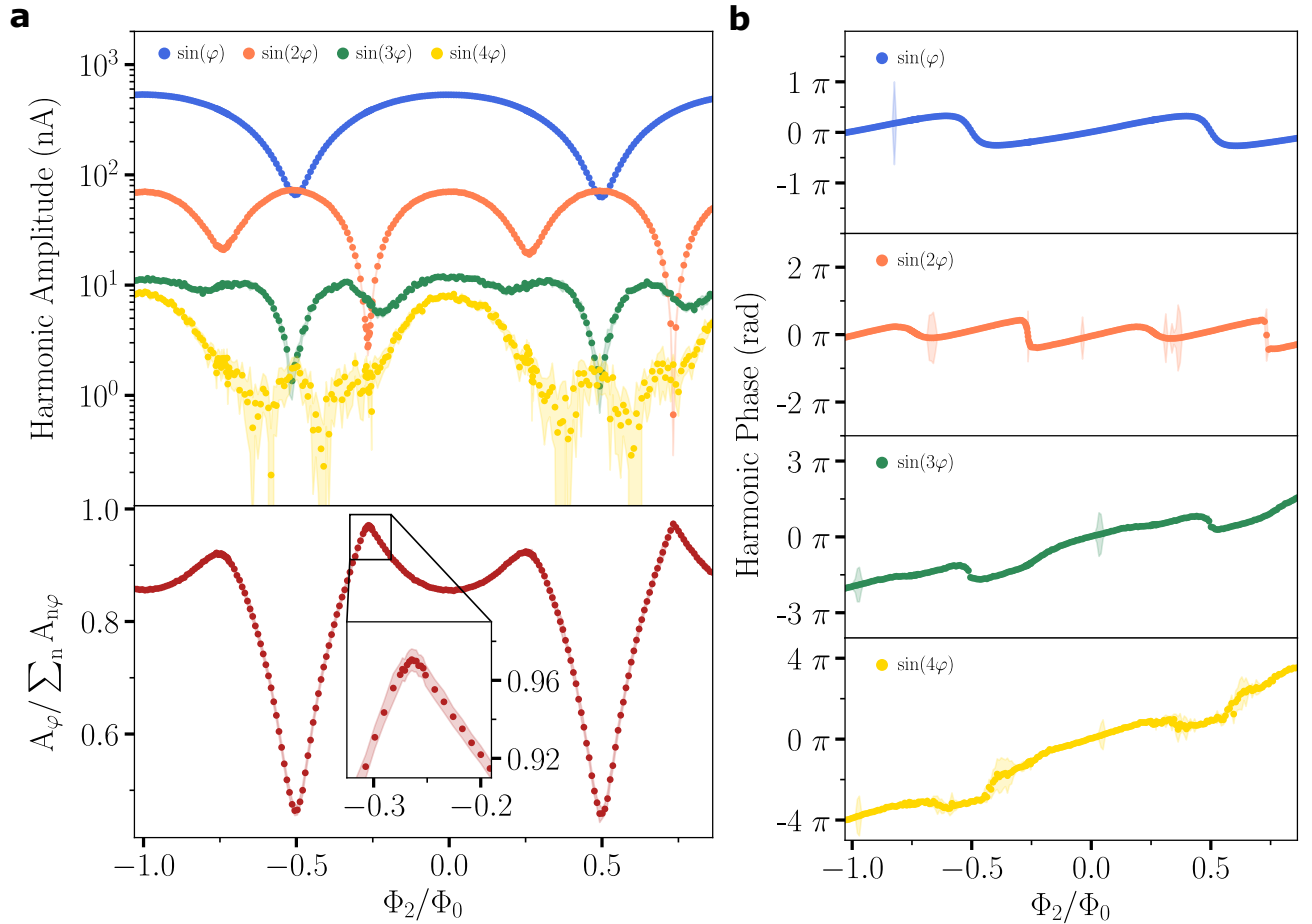


FIG. S8. **Nearly pure sinusoidal Josephson element.** The G-SQUID is tuned to make the second harmonics symmetric and thus maximize their cancellation at $\Phi_0/4$: $V_G^{N1} = -0.15$ V and $V_G^{N2} = -1.5$ V **a**, Upper panel: amplitude of each harmonic as function of the flux threading the G-SQUID loop. Lower panel: purity of the $\sin(\varphi)$ harmonic which reaches a value of $97.3 \pm 0.6\%$ when the second harmonic is cancelled out. **b**, Phase of each harmonic as function of Φ_2 .

S-VI. FLUX COMPENSATION

Two local flux lines permit the independent flux biasing of flux loops. The two flux lines are current biased at 4 K with a $4.7\text{ k}\Omega$ resistor as depicted in Fig. S8a,d. In order to estimate the cross-talk between the two fluxes we conduct two experiments. First, the small G-SQUID is isolated by pinching off J_W ($V_C^W = 2\text{ V}$) and the SQUID oscillations are measured by threading Φ_2 with V_1 (Fig. S8b) and with V_2 (Fig. S8c). Secondly, J_{N1} is pinched off to isolate an asymmetric SQUID comprising J_W and J_{N2} . Again, SQUID oscillations are measured by threading the loop with V_1 (Fig. S8e) and V_2 (Fig. S8f).

By superimposing, Fig. S8b with Fig. S8c and Fig. S8e with Fig. S8f we deduce the following compensation matrix:

$$\begin{bmatrix} V_{\Phi_1} \\ V_{\Phi_2} \end{bmatrix} = \begin{bmatrix} 1 & 0.0935 \\ 0.182 & 1 \end{bmatrix} \begin{bmatrix} V_1 \\ V_2 \end{bmatrix}$$

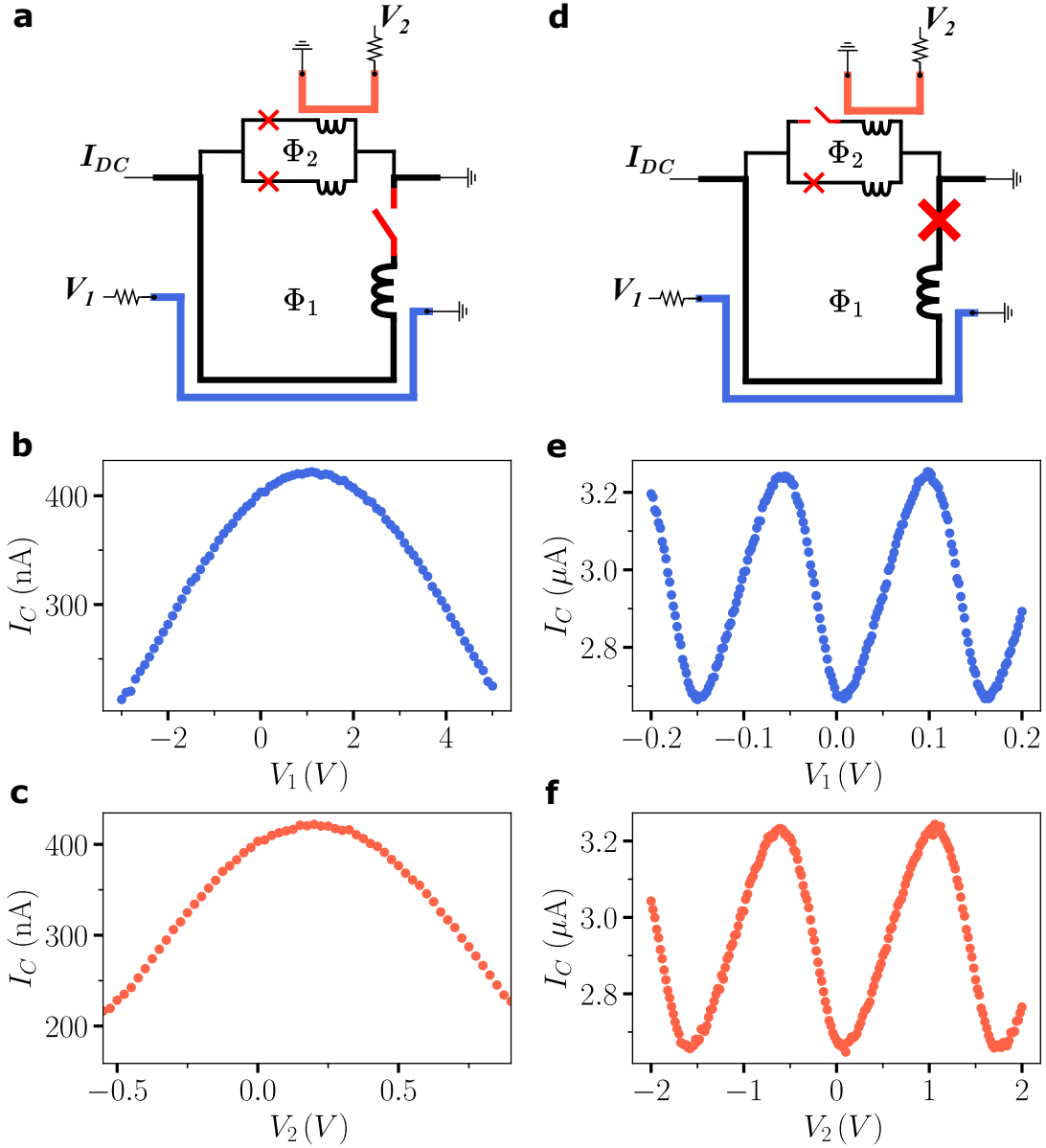


FIG. S9. **Flux cross-talk estimation.** **a**, The first configuration permits to explore the G-SQUID critical current oscillations as a function of the flux induced by each flux line **b** and **c**. **d**, The second configuration permits to measure the critical current oscillations of the SQUID formed by J_W and J_{N2} as a function of the flux induced by each flux line **e** and **f**.

S-VII. JOFETS THRESHOLD

As illustrated in Fig. 1c and c of the main text, the two narrow JoFETs embedded in the G-SQUID, J_{N1} and J_{N2} , exhibit a remarkably similar $I_C - V_G$ characteristic. However, a threshold voltage shift between the two is evident, as shown in Fig. S9. The critical currents are extracted from the data shown in Fig. 1c and d and presented in the Fig. S9 left panel. In the right panel, the critical current is plotted as a function of $V_G - V_{th}$, where V_{th} is the threshold voltage. By manual adjustment, we find $V_{th}^{N1} = 0.2$ V and $V_{th}^{N2} = 0.05$ V.

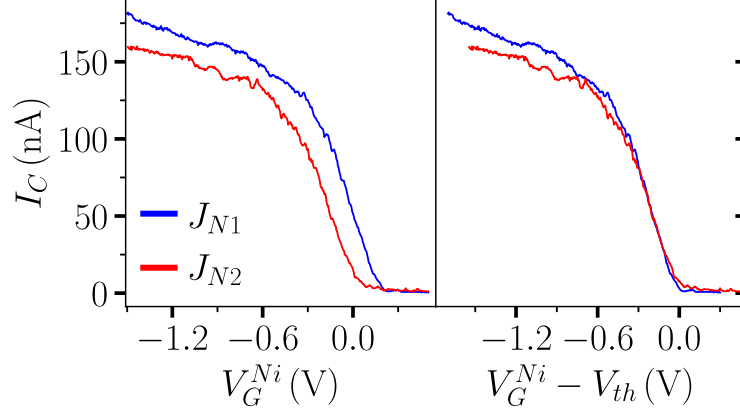


FIG. S10. **JoFETs threshold.** **Left**, J_{N1} and J_{N2} critical currents as a function of the gate voltage (extracted from the data shown in Fig.1c and d). **Right**, I_C as a function of $V_G - V_{th}$ where V_{th} is the threshold voltage. We find $V_{th}^{N1} = 0.2$ V and $V_{th}^{N2} = 0.05$ V.